HHS Public Access

Author manuscript

Ultrasound Med Biol. Author manuscript; available in PMC 2023 January 01.

Published in final edited form as:

Ultrasound Med Biol. 2023 January ; 49(1): 256–268. doi:10.1016/j.ultrasmedbio.2022.08.018.

COHERENCE METRICS FOR READER-INDEPENDENT DIFFERENTIATION OF CYSTIC FROM SOLID BREAST MASSES IN ULTRASOUND IMAGES

ALYCEN WIACEK[*], **ENIOLA OLUYEMI**[†], **KELLY MYERS**[†], **EMILY AMBINDER**[†], **MUYINATU A. LEDIJU BELL**[*,‡,§]

[*]Department of Electrical and Computer Engineering, Johns Hopkins University, Baltimore, Maryland, USA

[†]Department of Radiology and Radiological Science, Johns Hopkins Medicine, Baltimore, Maryland, USA

[‡]Department of Biomedical Engineering, Johns Hopkins University, Baltimore, Maryland, USA

[§]Department of Computer Science, Johns Hopkins University, Baltimore, Maryland, USA

Abstract

Traditional breast ultrasound imaging is a low-cost, real-time and portable method to assist with breast cancer screening and diagnosis, with particular benefits for patients with dense breast tissue. We previously demonstrated that incorporating coherence-based beamforming additionally improves the distinction of fluid-filled from solid breast masses, based on qualitative image interpretation by board-certified radiologists. However, variable sensitivity (range: 0.71–1.00 when detecting fluid-filled masses) was achieved by the individual radiologist readers. Therefore, we propose two objective coherence metrics, lag-one coherence (LOC) and coherence length (CL), to quantitatively determine the content of breast masses without requiring reader assessment. Data acquired from 31 breast masses were analyzed. Ideal separation (*i.e.,* 1.00 sensitivity and specificity) was achieved between fluid-filled and solid breast masses based on the mean or median LOC value within each mass. When separated based on mean and median CL values, the sensitivity/specificity decreased to 1.00/0.95 and 0.92/0.89, respectively. The greatest sensitivity and specificity were achieved in dense, rather than non-dense, breast tissue. These results support the introduction of an objective, reader-independent method for automated diagnoses of cystic breast masses.

Keywords

Breast ultrasound; Coherence-based beamforming; Complicated cysts; Breast cancer

Address correspondence to: awiacek@oakland.edu, mledijubell@jhu.edu.

Conflict of interest disclosure—The authors declare no competing interests.

INTRODUCTION

Breast cancer has been responsible for more than one-fourth of annual cancer diagnoses in women in the United States since 1999 (U.S. Cancer Statistics Working Group 2021), with approximately 287,850 new cases estimated in 2022 (Siegel et al. 2022). Early detection and diagnosis with assistance from breast ultrasound images are particularly important in patients with dense breast tissue, which reduces the sensitivity of mammography to mass or lesion detection (Mandelson et al. 2000). However, breast ultrasound has a high false-positive rate, resulting in many unnecessary biopsies or follow-up procedures of fluid-filled cysts (Berg et al. 2016) that could otherwise be diagnosed as Breast Imaging and Reporting Data System category 2 (BI-RADS 2) and dismissed as benign (Mendelson et al. 2001) if appropriately diagnosed as benign cysts at the time of diagnostic imaging.

One reason for the high false-positive rates of ultrasound is that fluid-filled cysts can appear similarly hypoechoic to solid masses because of image artifacts. For example, acoustic clutter is an artifact that results from a combination of multipath acoustic interactions, phase aberration and off-axis scattering (Lediju et al. 2008). Considering the heterogeneity of breast tissue, which increases the likelihood that multiple clutter-causing acoustic interactions will occur, the presence of acoustic clutter is particularly disruptive to breast ultrasound diagnoses.

Tissue harmonic imaging (THI) is the prevailing clinical option to remove acoustic clutter and possibly improve differentiation between fluid-filled cysts and solid masses (Szopinski et al. 2003). THI leverages non-linear wave propagation in tissue to create images from integer multiples of the transmitted frequency (Anvari et al. 2015). In breast imaging, THI improves lesion conspicuity and margin assessment, particularly for fluid-filled masses (Rosen and Soo 2001). However, the benefits of THI are reduced within breast tissue that is not purely fatty (Mesurolle et al. 2006), such as increased shadowing in the presence of denser tissue (Cha et al. 2007) and decreased penetration depth with the use of higher frequencies.

Quantitative ultrasound (QUS) extracts features from radiofrequency (RF) data to characterize breast lesions using methods such as the backscatter coefficient, effective scatterer diameter and effective acoustic concentration (Shankar et al. 2001; Oelze et al. 2007; Nam et al. 2013; Sadeghi-Naini et al. 2013; Trop et al. 2014; Sannachi et al. 2015). However, these methods require careful calibration with a reference phantom and are often computationally complex.

Quantitative transmission (QT) ultrasound is an emerging imaging approach capable of creating 3-D maps of breast tissue properties (*e.g.,* sound speed) by transmitting a plane wave that is received on the opposite side of the breast (Lenox et al. 2015). This approach has been used to classify breast tissue (Malik et al. 2016), differentiate between fluid and solid masses (Iuanow et al. 2017), and calculate the speed of sound within breast cysts to aid in clinical management (Malik and Klock 2019). Breast tissue was classified as skin, fat, glands, ducts or connective tissue (Malik et al. 2016). Fluid and solid mass contents were successfully differentiated in a reader study consisting of 37 breast lesions and 14 readers

who classified whether a lesion was a cyst or solid mass (Iuanow et al. 2017). Calculated sound speeds in large cysts correlated with the cytological features of fluid samples taken from within the cyst (Malik and Klock 2019). These QT ultrasound systems offer both reflection and transmission measurements; however, they require ultrasound transducers integrated with specialized patient tables, complex tomographic hardware, and acquisition times of 5–10 min (Malik and Klock 2019). These features reduce the overall portability, cost-effectiveness, and real-time benefits that have traditionally been mainstay advantages of ultrasound technology.

Previous studies have also leveraged the temporal correlation of speckle associated with pre- and post-compression images to differentiate cysts from solid lesions in breast tissue. These methods belong to a class of imaging known as elastography, in which tissue is manually compressed, followed by motion tracking to measure tissue elasticity responses post-compression. For example, Booi et al. (2007, 2008) used a 2-D phase-sensitive speckle tracking algorithm to demonstrate that the resulting temporal correlation coefficients from cysts were considerably lower than those from surrounding tissue. Because of the absence of speckle within fluid-filled lesions, many elastography methods fail to produce images of fluid-filled lesions. Therefore, also looking at speckle, other studies proposed combined elastography images (Nahiyan and Hasan 2015; Rabbi and Hasan 2017), which differentiate cystic from solid masses based on signal amplitude, temporal correlation coefficients between pre- and post-compression signals, and comparisons when the same signal processing is applied to surrounding tissue. However, difficulties locating small lesions, as well as misidentification of fluid-filled regions, were noted (Nahiyan and Hasan 2015).

Rather than manual compression, previous studies used acoustic radiation force (ARF) excitation to induce local fluidic motion (*i.e.,* acoustic streaming), followed by tracking methods to detect the induced motion and thereby distinguish fluid from solid masses (Nightingale et al. 1999; Soo et al. 2006; Doherty et al. 2013). Solid masses did not respond to this ARF excitation, resulting in a cyst detection sensitivity and specificity of 0.50 and 1.00, respectively, for a population of 21 indeterminate lesions (Soo et al. 2006). Similarly, Phillips et al. (2021) introduced an ARF impulse imaging method to locally deform tissue, temporally correlate responses to the induced motion and thereby determine the content of breast masses. The associated delta log variance of acceleration, ΔLog(VoA), produced lower values in fluid-filled masses compared with solid masses due to the elastic recovery of solid tissue compared with the slower recovery of fluid. However, this entire class of ARF-based methods requires specialized equipment capable of generating the required high-energy, high-intensity, focused excitation pulses, and the accuracy of results also depends on loading conditions introduced by the probe pressure required to maintain acoustic coupling and contact (Barr 2012; Barr and Zhang 2012; Balleyguier et al. 2013; Bell et al. 2015).

As an alternative to compression- or ARF-based methods, our previous work investigated the first applications of coherence-based beamforming to breast tissue, demonstrating that spatial (rather than temporal) coherence has the potential to improve differentiation of fluid-filled from solid breast masses (Wiacek et al. 2018a, 2018b). A reader study was then performed with 26 masses and five board-certified radiologists to determine the clinical

advantages of robust short-lag spatial coherence (R-SLSC) (Nair et al. 2018; Wiacek et al. 2020c). The mean percentage of fluid-filled masses correctly assessed as BI-RADS 2 increased from 32% with traditional ultrasound B-mode imaging to 63% with the inclusion of R-SLSC imaging (Wiacek et al. 2020b, 2020c). However, the requirement for reader assessment resulted in fluid detection sensitivity ranging 0.71 to 1.00 based on the reader, which indicates that the mean increase in BI-RADS 2 diagnoses could have been greater if more readers achieved greater sensitivity. It is also notable that individual reader sensitivity did not correlate with radiologist experience.

To maximize the clinical benefits of coherence-based beamforming for breast ultrasound applications, we are investigating the use of two quantitative coherence metrics that will objectively determine the content of breast masses without requiring subjective reader input: lag-one coherence (LOC) and coherence length (CL). We build on our previous conference publications using LOC and CL to classify breast mass contents as fluid or solid (Wiacek et al. 2020b, 2021b), which had a sensitivity and specificity of fluid-filled mass detection ranging from 0.768 to 1.00 and from 0.688 to 0.94, respectively. The novel contributions of this work include a larger data set supporting our initial observations, a more detailed analysis of the distribution of LOC and CL values within breast masses, a preliminary assessment of critical relationships (*i.e.,* among LOC, CL, mass type, and breast density) and suggestions for clinical implementation.

The remainder of this article is structured as follows. We describe the rationale of our approach, our inclusion and exclusion criteria, and our data analysis methods. The study results are then presented, followed by a discussion of our key contributions. The article concludes with a summary of the clinical promise of the proposed approach.

METHODS

LOC and CL as objective discriminators of fluid or solid mass content

Spatial coherence in ultrasound can be described as a measurement of the similarity of backscattered ultrasound waves as a function of element spacing, or lag. This measurement can produce a normalized spatial coherence function, $\widehat{R}$, which is the basis for short-lag spatial coherence (SLSC) imaging (Lediju et al. 2011):

$$\widehat{R}[m] = \frac{1}{N-m}\sum_{i=1}^{N-m}\frac{\sum_{n=n_1}^{n_2} s_i[n]s_{i+m}[n]}{\sqrt{\sum_{n=n_1}^{n_2} s_i^2[n]\sum_{n=n_1}^{n_2} s_{i+m}^2[n]}}, \quad (1)$$

Here, m is the spatial lag, represented as the number of elements between two points being spatially correlated; N is the number of elements in the transducer; $s_i[n]$ is a time-delayed, zero-mean signal received at element i from depth n; and n_1 and n_2 represent axial positions, where $n_1 - n_2$ is the size of the axial correlation kernel.

The presence of spatially incoherent noise produces a delta-like function at lag $m = 0$ of the coherence function (Long et al. 2018). This delta-like function scales in magnitude based on the relative noise power. Rather than using eqn (1) to create a range of previously

reported coherence-based images (Lediju et al. 2011; Gonzalez and Bell 2018; Nair et al. 2018), a method that considers only immediately neighboring elements (*i.e.,* m =1, also known as lag-one coherence, or LOC) sufficiently characterizes the presence of spatially incoherent signals by measuring the decorrelation resulting from the delta-like function. This incoherent signal is a result of thermal noise, reverberation clutter, and high-frequency aberration.

The presence of a delta-like function also affects the CL, which is the first zero-crossing of $\hat{R}[m]$. Ideally, the coherence function within a tissue region would be a triangular function of width N–1, as predicted by the van Cittert–Zernike theorem (Mallart and Fink 1991; Goodman 2015), resulting in an ideal CL of N–1. However, the rapid decorrelation at short lags caused by the presence of incoherent signals translates to significantly shorter CLs that deviate from the ideal value.

Although LOC was introduced as a measurement of image quality (Long et al. 2018, 2020), we propose LOC as a method to classify the content of breast lesions as solid or fluid, considering its ability to quantify the presence of spatially incoherent signal within breast masses. This rationale extends to CL. Because fluid-filled lesions are expected to lack scatterers that provide backscattered signals, a low LOC or short CL is anticipated. Conversely, a higher LOC or longer CL is expected to indicate the presence of a solid mass. In addition, as breast density increases, there are increased layers of fibroglandular tissue, resulting in increased levels of acoustic clutter and spatially incoherent signal. Therefore, we expect improved differentiation of fluid and solid masses within dense breast tissue compared with non-dense breast tissue when using LOC and CL as discriminators of mass contents.

Data acquisition

Twenty-seven patients scheduled for ultrasound-guided aspiration or core-needle biopsy were included in our study after informed consent and approval from the Johns Hopkins Medicine Institutional Review Board (Protocol No. IRB00127110). Each patient had at least one suspicious hypoechoic breast mass, resulting in 31 total masses included in this study. Patients ranged from 20 to 80 y in age, with a mean age of 55 y. Each patient was imaged by a board-certified breast radiologist with experience beyond residency ranging 2 to 7 y. The ultrasound transducer was either an L3–8 or L8–17 linear array with a center frequency of 5.5 or 12.5 MHz, respectively, connected to an Alpinion ECUBE-12R ultrasound scanner (Alpinion, Seoul, Korea) with combined clinical and research data acquisition capabilities. Each acquisition consisted of focused transmissions with a 64-element receive aperture. Raw RF ultrasound data were acquired and saved for post-procedure processing. In addition to the RF data, clinical screenshots of ultrasound B-mode images located within the same buffer as the RF data were concurrently acquired to aid in mass identification. For masses that were difficult to identify, the mass was annotated by the scanning radiologist and a subsequent screenshot was acquired.

For masses where the differential diagnosis included a cyst, ultrasound-guided aspiration was initially attempted. Upon successful aspiration, the mass was classified as a cyst. Three simple cysts were present in addition to the masses scheduled for aspiration or

biopsy, and were classified as cysts without aspiration because of clinical B-mode ultrasound features matching a simple cyst. For the remaining masses, the results of each core-needle biopsy served as the ground truth for mass classification. In cases in which surgical excision was performed, this ground truth was updated to represent the surgical pathology. According to these ground truths, the included masses consisted of 12 fluid-filled simple and complicated cysts, 11 benign solid masses (*e. g.,* fibroadenoma) and 8 malignant solid masses (*e.g.,* invasive ductal carcinoma, ductal carcinoma in situ). Masses determined to have a combination of fluid and solid components were excluded from this study.

Patient medical records were referenced retrospectively to determine breast density based on the most recent mammogram at the time of ultrasound data acquisition. In clinical practice, mammographic breast density is divided into four categories (Spak et al. 2017): (A) almost entirely fat, (B) scattered fibroglandular densities, (C) heterogeneously dense and (D) extremely dense. For masses that met our inclusion criteria, none of the surrounding breast tissue densities were characterized as A, and there were no fluid masses surrounded by tissue characterized as D. Therefore, to complete our analysis, we reduced the granularity of these categories by defining non-dense breast tissue as B (consisting of six fluid and seven solid masses) and dense breast tissue as the combination of C (six fluid and eight solid masses) and D (four solid masses). Table 1 summarizes the number of masses with fluid or solid content and surrounding breast tissue densities included in this study. Patients with no prior mammogram were excluded from this study because mammographic breast density was unknown.

Data analysis

The acquired RF data were processed using delay-and-sum (DAS) beamforming to create an image comparable to the traditional clinical image. Equation (1) was then evaluated with axial kernels (*i.e.,* $k = n_1 - n_2$) equivalent to one acoustic wavelength, resulting in LOC and CL values for each pixel in the traditional DAS image. Relying solely on the DAS image, for each mass, a region of interest (ROI) was manually defined within the mass, intentionally avoiding the edges of the mass to avoid confounding effects from the mass boundaries. This ROI (confirmed by visualizing the clinical screenshot and/or associated annotated screenshot) was used to determine corresponding LOC and CL values within the mass. For each mass, coherence metric distribution statistics were computed using three methods to provide a complete understanding of the central tendency of the LOC and CL distributions within the ROI and to avoid a biased estimate of the central tendency caused by potential outlier values within the distribution: (i) all values within the ROI, (ii) the mean of all values in the ROI, and (iii) the median of all values in the ROI. Finally, each of these distribution statistics was stratified by mass type (*i.e.,* fluid or solid) and breast tissue density (*i.e.,* dense or non-dense).

To objectively distinguish solid from fluid breast masses, the LOC threshold for fluid-filled mass detection was varied from −1 to 1 in increments of 0.01, and the CL threshold for fluid-filled mass detection was varied from 0 to 63 in increments of 1. At each incremental LOC or CL threshold, the distribution statistic for each mass was classified as solid or fluid based on an LOC or CL value above or below the threshold, respectively. This process

was repeated for the three distribution statistics noted above (*i.e.,* all, mean, and median). Histograms were created with 50 bins spanning −1 to 1 to visualize LOC distributions and with 64 bins spanning 0 to 63 to visualize CL distributions. The level of overlap between these histograms from fluid and solid masses was subjectively described on a scale ranging from minimal to moderate to considerable, with statistical reports of sensitivity and specificity serving as the corresponding objective measurements of overlap.

To mimic a clinical scenario where an LOC or CL threshold is established based on previous patient data and a new patient presents in the clinic for ultrasound evaluation, a leave-one-out cross-validation analysis was performed. Specifically, with one mass held out for validation, the LOC or CL threshold was determined based on a training set containing the remaining masses. This process was repeated for each mass, and accuracy was determined by comparing the predicted diagnosis with the ground truth for each of these validation sets. Figure 1 presents a graphical illustration of the connection between this validation method and the proposed clinical workflow. From this perspective, the determined LOC or CL thresholds for each training set were recorded, and the means ± one standard deviation of these thresholds were reported to represent expectations when these thresholds are determined from different combinations of patients.

Statistical analysis

The sensitivity and specificity of fluid mass detection were measured as

$$\text{Sensitivity} = \frac{TP}{TP + FN} \tag{2}$$

$$\text{Specificity} = \frac{TN}{TN + FP} \tag{3}$$

where a true positive (TP) or false negative (FN) was defined as a pixel within a fluid-filled mass with a distribution statistic below or above the threshold, respectively. A TN or FP was defined as a pixel within a solid mass with a distribution statistic above or below the threshold, respectively. In this context, sensitivity measures the fraction of fluid masses correctly classified as fluid, while specificity measures the fraction of solid masses correctly classified as solid.

With these measurements, a receiver operating characteristic (ROC) curve was used to determine the optimal LOC and CL threshold values by measuring the distance to the ideal operating point of (0,1). In particular, for each LOC or CL threshold value discretized using the same increments described above, the distance from the respective point on the receiver operating characteristic (ROC) curve to (0,1) was measured, and the LOC or CL threshold value resulting in the minimum distance was selected as optimal. When multiple possible thresholds yielded distances equivalent to the minimum distance, the minimum LOC or CL threshold was selected as optimal. This optimal threshold selection represents a conservative diagnostic approach where the threshold is set such that a diagnosis of solid (*i.e.,* above the threshold) is preferred over a diagnosis of fluid (*i.e.,* below the threshold) to avoid missed

cancers. In addition, the area under the ROC curve (AUC) was estimated using trapezoidal numerical integration.

RESULTS

Spatial coherence distributions within individual masses

Figure 2 displays violin plots visualizing the distribution of LOC (top) and CL (bottom) values for each mass included in this study. Based on the LOC distributions, there is some overlap between the LOC distributions of fluid and solid masses. However, each mean or median LOC for each fluid mass lies below the threshold determined from all LOC values, each mean LOC for each solid mass exceeds this threshold and a majority of solid masses (*i.e.,* 17/19) produce median LOC values that exceed the threshold. The LOC values for simple and complicated cysts overlap, as noted by cross-referencing Figure 2 with Table 2.

The CL distributions in Figure 2 show more overlap between solid and fluid masses when compared with the LOC distributions. To better visualize the differences between the mean and median, the y-axis was clipped at 20, although many of the masses have additional values beyond 20, with outliers up to a maximum value of 63. Of the 12 fluid-filled masses, 7 and 11 produced mean and median CL values, respectively, that do not exceed the CL threshold determined from all CL values. Of the 19 solid masses, 18 and 16 produced mean and median CL values, respectively, that exceed the CL threshold. Therefore, a majority of masses produce CLs that confer with the observed trend of fluid-filled masses not exceeding and solid masses exceeding the CL threshold, although this trend is not completely reliable for all masses. The CL values for simple cysts and complicated cysts overlap, as noted by cross-referencing Figure 2 with Table 2.

LOC of all masses

Figure 3 shows the LOC separation between fluid-filled and solid masses for all masses included in our study (top), for all masses surrounded by non-dense tissue (middle), and for all masses surrounded by dense tissue (bottom). The left column shows histograms of all LOC values within either fluid or solid masses. The middle column shows violin plots of the LOC distribution for the three distribution statistics (*i.e.,* all, mean, median). The right column shows corresponding ROC curves.

The top left of Figure 3 shows that there is moderate overlap between the histograms, representing a sensitivity and specificity of 0.85 and 0.87, respectively. When considering either the mean or median LOC value, there is complete separation between solid and fluid masses, as shown in Figure 3 (top center). This complete separation results in 1.00 sensitivity and 1.00 specificity for fluid-filled mass detection in each case. The corresponding ROC curves indicate that the optimal LOC thresholds for fluid-filled mass detection are 0.28, 0.28 and 0.27 when using all, mean and median LOC values, respectively.

LOC of masses surrounded by non-dense breast tissue

The middle left of Figure 3 shows considerable overlap between the distribution of LOC values in fluid and solid masses surrounded by non-dense breast tissue. This overlap results in a sensitivity and specificity of 0.79 and 0.77, respectively. Despite this overlap, when the mean or median LOC values are used, there is complete separation between solid and fluid masses, as shown in Figure 3 (center). The corresponding ROC curves indicate that the optimal LOC thresholds for fluid-filled mass detection are 0.33, 0.28, and 0.27 when using all, mean and median LOC values, respectively.

LOC of masses surrounded by dense breast tissue

The bottom left of Figure 3 shows minimal overlap between the distribution of LOC values in fluid and solid masses surrounded by dense breast tissue, resulting in a sensitivity and specificity of 0.95 and 0.95, respectively. Similar to the results for non-dense breasts and all masses, when using the mean and median LOC values, there is complete separation between solid and fluid masses, as shown in Figure 3 (bottom center), resulting in 1.00 sensitivity and 1.00 specificity for fluid-filled mass detection based on both the mean and median LOC. The corresponding ROC curves indicate that the optimal LOC thresholds for fluid-filled mass detection are 0.21, 0.12 and 0.12 when using all, mean and median LOC values, respectively.

Although the mean and median LOC values offer ideal separation between fluid and solid masses within both dense and non-dense breast tissue, the distance between the distributions, and therefore the separation between fluid and solid masses, is greater in masses within dense breast tissue. In addition, the optimal LOC threshold for distinguishing fluid-filled from solid masses was lower in dense tissue (*i.e.,* 0.21) than in non-dense tissue (*i.e.,* 0.33). The AUCs associated with these categories of datasets are reported in Table 3.

CL of all masses

Figure 4 shows the CL separation between fluid-filled and solid masses for all masses included in our study (top), for all masses surrounded by non-dense tissue (middle), and for all masses surrounded by dense tissue (bottom). The left column shows histograms of all CL values within either fluid or solid masses. The middle column shows violin plots of the CL distribution for the three distribution statistics (*i.e.,* all, mean, median). The right column shows corresponding ROC curves. Additional CL results are reported in Table 3.

The top left of Figure 4 shows that there is moderate overlap between the distribution of CL values in fluid and solid masses. These distributions both appear to approximately follow a Rayleigh distribution as opposed to the approximate Gaussian distributions seen in Figure 3 for LOC. Specifically in the distribution of fluid masses, there is a large probability in the first bin, which represents a coherence length of zero. This means the coherence function does not cross zero and is likely an indication of noise. The distribution of CL values in solid masses have a shifted distribution compared with that of CL values in fluid masses, representing a larger CL for solid masses despite the moderate overlap between the distributions. This overlap represents a sensitivity and specificity of 0.76 and 0.87, respectively for all CL values.

When considering discrimination between solid and fluid masses based on the mean CL values, the sensitivity and specificity for fluid mass detection are 1.00 and 0.95, respectively. The ability to make this distinction decreases when the median CL values are instead used as a discriminator, resulting in 0.92 sensitivity and 0.89 specificity, as shown in Figure 4 (top center). The corresponding ROC curves indicate that the optimal CL thresholds for fluid-filled mass detection are 3, 6 and 3 when using all, mean and median CL values, respectively.

CL of masses surrounded by non-dense breast tissue

The middle left of Figure 4 shows considerable overlap between the distribution of CL values in fluid and solid masses surrounded by non-dense breast tissue. This overlap results in 0.63 sensitivity and 0.79 specificity. When considering the mean CL values, the separation improves, resulting in a 1.00 sensitivity and 0.86 specificity. When the median CL values are used as the discriminator, the sensitivity and specificity are 0.83 and 0.86, respectively, resulting in a separation between solid and fluid masses worse than that achieved with the mean CL values, as shown in Figure 4 (center). The corresponding ROC curves indicate that the optimal CL thresholds for fluid-filled mass detection are 3, 6 and 3 when using all, mean and median CL values, respectively.

CL of masses surrounded by dense breast tissue

The bottom left of Figure 4 shows minimal overlap between the distribution of CL values in fluid and solid masses, resulting in a 0.87 sensitivity and 0.91 specificity. When the mean and median CL values are used as discriminators, there is complete separation between solid and fluid masses, as shown in Figure 4 (bottom center), resulting in a 1.00 sensitivity and 1.00 specificity for fluid-filled mass detection based on both the mean and median CL. The corresponding ROC curves indicate that the optimal LOC thresholds for fluid-filled mass detection are 3, 4 and 3 when using all, mean and median CL values, respectively.

Comparison with reader performance

Table 3 compares the LOC and CL sensitivity and specificity for each breast tissue density and distribution statistic reported in Figures 3 and 4 with the sensitivity and specificity achieved in two previous reader studies distinguishing solid and fluid-filled breast masses (Iuanow et al. 2017; Wiacek et al. 2020c). In Wiacek et al. (2020c), readers focused on making this distinction with assistance from R-SLSC images, while the readers in Iuanow et al. (2017) focused on making this distinction based on QT ultrasound images. Without requiring any reader input, the objective LOC discriminator metric improved the sensitivity and specificity of distinguishing fluid from solid masses based on mean or median LOC values, as compared with these two recently introduced methods (*i.e.,* mean sensitivity improved from 0.86–0.93 to 1.00, and mean specificity improved from 0.86–0.95 to 1.00). In addition, similar sensitivity and specificity to those of the two recently introduced methods were achieved when separating on the basis of all LOC values (*i.e.,* 0.85–0.93 mean sensitivity and 0.86–0.95 mean specificity). Finally, using mean CL values improved mean sensitivity (from 0.86–0.93 to 1.00) with similar mean specificity (*i.e.,* 0.86–0.95) when compared with the R-SLSC and QT ultrasound approaches to distinguishing fluid from solid masses. The remaining CL metrics comparisons (*i.e.,* all CL values, median CL

values) produce a sensitivity or specificity similar to or worse than that of R-SLSC or QT ultrasound, with the exception of the 1.00 sensitivity and 1.00 specificity achieved with median CL values for masses surrounded by dense breast tissue.

Cross-validation to assess robustness and clinical utility

Table 4 reports the results of the leave-one-out cross-validation analysis. Specifically, the best accuracy (*i.e.,* 96.8%) was achieved using mean or median LOC distribution statistics, where only one fluid mass was incorrectly classified as solid. With one mass left out, the optimal thresholds were determined based on the remaining masses resulting in LOC and CL threshold standard deviations of <0.006 and <0.4, respectively. These standard deviations represent 0.68%–1.96% of the reported LOC thresholds and 3.01%–7.93% of the reported CL thresholds, which demonstrates robustness regardless of the specific patients included or excluded when determining these LOC and CL thresholds.

Figure 5 shows example B-mode and LOC images of solid and fluid-filled masses surrounded by dense and non-dense breast tissue. These examples provide qualitative representations of the differentiation between fluid and solid masses that may be implemented clinically in addition to the quantitative reports noted above. Only LOC images are shown, given the improved performance of LOC compared with CL reported above. The center of the color scale of each LOC image was set to be the optimal threshold determined from all measured LOCs of all masses (*i.e.,* 0.28), which enables the color for each pixel to represent a prediction of whether the indicated pixel is solid or fluid. The top (*i.e.,* <5 mm axial depth) of each LOC image is *blue* because this region resides outside of the transmit focal zone (Lediju et al. 2011), and this feature can possibly be used to confirm the expected contrast between fluid or solid masses and nearby surrounding tissue.

DISCUSSION

This study is the first to investigate two quantitative coherence-based metrics to objectively diagnose the fluid or solid content of 31 breast masses in ultrasound. Based on the assumption that fluid-filled masses have minimal to non-existent acoustic scatterers, the majority of high-amplitude content appearing within fluid-filled masses is expected to be caused by incoherent noise and acoustic clutter. Therefore, the coherence-based LOC and CL metrics enable objective quantification of incoherent noise and acoustic clutter. The results in Table 3 reveal the clinical potential of these metrics to directly diagnose fluid-filled masses as BI-RADS 2 (*i.e.,* benign) and thereby avoid additional follow-up or biopsies because of the complete separation between solid and fluid masses. This potential is particularly beneficial for patients with dense breast tissue (see Figs. 3 and 4), a subclass of patients who are most commonly referred for supplemental breast cancer screening with ultrasound. This finding is additionally remarkable because the majority of these fluid-filled masses were difficult to diagnose with clinical ultrasound B-mode images and required biopsy or aspiration as part of clinical management.

Three additional advantages to the proposed LOC or CL implementation immediately follow. First, both LOC and CL are quantitative values that can be provided as a threshold, similarly to quantitative elasticity parameters in elastography (Blank and Antaki

2017), enabling simpler interpretation and integration into the breast clinic. Second, the rationale for the proposed approach directly connects to the physics of ultrasound backscatter principles and theory, which further simplifies technical understanding, clinical interpretation and radiologist integration. Third, in comparison to previously reported methods (*e.g.,* speckle correlation, ARF-based methods, QT ultrasound, QUS), the proposed approach does not require compression, deformation, high-energy pulses, controlled loading conditions, alterations to the standard clinical ultrasound transmit beam sequence, calibration with a reference phantom, or dedicated hardware that minimizes cost-effectiveness and portability. These benefits combine to enhance the promise of deploying the proposed technique in remote or resource-limited locations and on wireless ultrasound systems (Faruk et al. 2015; Dietrich et al. 2017; Shin et al. 2018; Wildeboer et al. 2019).

Qualitative LOC images were presented as a supplement to quantitative image values (see Fig. 5). Although these LOC images differ from traditional B-mode images, they have the potential to aid the transition from traditional image interpretation to a single objective number that summarizes the presence of solid or fluid mass content. Alternatively, the LOC image could be presented as an overlay, similar to previously presented R-SLSC overlays (Wiacek et al. 2018a, 2018b).

We presented three possible distribution statistics (*i.e.,* all, mean, and median). After considering these multiple options, we recommend using the mean or median LOCs within an ROI to differentiate solid from fluid masses, given the complete separation of the respective distributions (see top center of Fig. 3) and the greatest sensitivity, specificity and accuracy (see Tables 3 and 4), which is highly promising for the proposed approach. When compared with previous studies using qualitative R-SLSC images and QT ultrasound, LOC offered improved sensitivity and specificity without requiring reader input (see Table 3).

The leave-one-out cross-validation analysis simulates several clinical scenarios where a LOC or CL threshold could be set based on prior patient data and a new patient is assessed based on the pre-determined threshold. The 96.8% LOC accuracy reported in Table 4 suggests that there is strong potential for clinical utility and impact. In these clinical scenarios, all malignant masses would have been biopsied correctly and only one fluid mass would have been unnecessarily biopsied (which is the preferred clinical scenario compared with a solid mass incorrectly classified as fluid). In addition, the selected LOC and CL thresholds for each training set produced standard deviations (see Table 4) that were 0.68%–1.96% and 3.01%–7.93% of the mean LOC and CL values, respectively. These standard deviations further support the suggestion that LOC is a robust indicator of lesion contents. Including additional patient data to set this threshold may further increase the robustness of both LOC and CL in discriminating mass contents. With additional data, Figure 3 also indicates that specific thresholds can possibly be defined based on mammographic breast density.

Providing a more forward-thinking viewpoint, LOC and CL have the potential to advance computer-aided diagnostic systems to automate BI-RADS 2 classification of fluid-filled cysts. In addition, the recently introduced CohereNet architecture could also be used to

introduce additional automation and reduce the computational complexity of coherence calculations (Wiacek et al. 2019, 2020a, 2021a). One limitation to complete user independence is that manual ROIs were defined to measure LOC and CL, which requires radiologist intervention during imaging. However, this manual intervention can potentially be replaced with traditional or deep learning-based (Nair et al. 2020) ultrasound image segmentation algorithms.

CONCLUSIONS

This article summarizes the impact of using two quantitative coherence-based metrics, LOC and CL, to distinguish fluid from solid breast masses. When introduced as a standalone diagnostic parameter, the mean or median LOC within ROIs of each mass produced ideal separations between fluid and solid breast masses with a sensitivity and specificity of 1.00. Similarly, when considering the mean CL within ROIs of each mass, the sensitivity and specificity of fluid mass detection were 1.00 and 0.95, respectively. In addition, the separation between fluid and solid masses was overwhelmingly improved when masses were surrounded by dense breast tissue. These results provide a promising framework to include quantitative coherence-based metrics into the breast clinic, particularly as a method to eliminate reader subjectivity, objectively diagnose BI-RADS 2 masses, and eliminate the need for biopsy or follow-up of these fluid-filled masses.

Acknowledgments—

Funding for this research was provided by the Oak Ridge Associated Universities (ORAU) Ralph E. Powe Junior Faculty Enhancement Award and the National Institute of Biomedical Imaging and Bioengineering of the National Institutes of Health under Award No. R01EB032960 (both awarded to M.A.L.B.). A.W. is a recipient of the 2021–2022 Achievement Rewards for College Scientists (ARCS) Foundation Scholarship and the 2022 Siebel Scholarship.

REFERENCES

Anvari A, Forsberg F, Samir AE. A primer on the physical principles of tissue harmonic imaging. Radiographics 2015;35:1955–1964. [PubMed: 26562232]

Balleyguier C, Canale S, Hassen WB, Vielh P, Bayou E, Mathieu M, Uzan C, Bourgier C, Dromain C. Breast elasticity: Principles, technique, results: An update and overview of commercially available software. Eur J Radiol 2013;82:427–434. [PubMed: 22445593]

Barr RG. Shear wave imaging of the breast: still on the learning curve. J Ultrasound Med 2012;31:347–350. [PubMed: 22368124]

Barr RG, Zhang Z. Effects of precompression on elasticity imaging of the breast: development of a clinically useful semiquantitative method of precompression assessment. J Ultrasound Med 2012;31: 895–902. [PubMed: 22644686]

Bell MAL, Kumar S, Kuo L, Sen HT, Lordachita I, Kazanzides P. Toward standardized acoustic radiation force (ARF)-based ultrasound elasticity measurements with robotic force control. IEEE Trans Biomed Eng 2015;63:1517–1524. [PubMed: 26552071]

Berg WA, Bandos AI, Mendelson EB, Lehrer D, Jong RA, Pisano ED. Ultrasound as the primary screening test for breast cancer: Analysis from ACRIN 6666. J Natl Cancer Inst 2016;108:djv367.

Blank MA, Antaki JF. Breast lesion elastography region of interest selection and quantitative heterogeneity: A systematic review and meta-analysis. Ultrasound Med Biol 2017;43:387–397. [PubMed: 27746010]

Booi RC, Carson PL, O'Donnell M, Richards MS, Rubin JM. Diagnosing cysts with correlation coefficient images from 2-dimensional freehand elastography. J Ultrasound Med 2007;26: 1201–1207. [PubMed: 17715314]

Booi RC, Carson PL, O'Donnell M, Roubidoux MA, Hall AL, Rubin JM. Characterization of cysts using differential correlation coefficient values from two-dimensional breast elastography: Preliminary study. Ultrasound Med Biol 2008;34:12–21. [PubMed: 17900795]

Cha JH, Moon WK, Cho N, Kim SM, Park SH, Han BK, Choe YH, Park JM, Im JG. Characterization of benign and malignant solid breast masses: Comparison of conventional US and tissue harmonic imaging. Radiology 2007;242:63–69. [PubMed: 17090709]

Dietrich CF, Goudie A, Chiorean L, Cui XW, Gilja OH, Dong Y, Abramowicz JS, Vinayak S, Westerway SC, Nolsøe CP, Chou YH, Blaivas M. Point of care ultrasound: A WFUMB position paper. Ultrasound Med Biol 2017;43:49–58. [PubMed: 27472989]

Doherty JR, Trahey GE, Nightingale KR, Palmeri ML. Acoustic radiation force elasticity imaging in diagnostic ultrasound. IEEE Trans Ultrason Ferroelectr Freq Control 2013;60:685–701. [PubMed: 23549529]

Faruk T, Islam MK, Arefin S, Haq MZ. The journey of elastography: Background, current status, and future possibilities in breast cancer diagnosis. Clin Breast Cancer 2015;15:313–324. [PubMed: 25858446]

Gonzalez E, Bell MAL. Segmenting bone structures in ultrasound images with locally weighted SLSC (LW-SLSC) beamforming. Proc IEEE Int Ultrason Symp 2018;1–9.

Goodman JW. Statistical optics. New York: Wiley; 2015.

Iuanow E, Smith K, Obuchowski NA, Bullen J, Klock JC. Accuracy of cyst versus solid diagnosis in the breast using quantitative transmission (QT) ultrasound. Acad Radiol 2017;24:1148–1153. [PubMed: 28549870]

Lediju MA, Pihl MJ, Dahl JJ, Trahey GE. Quantitative assessment of the magnitude, impact and spatial extent of ultrasonic clutter. Ultrason Imaging 2008;30:151–168. [PubMed: 19149461]

Lediju MA, Trahey GE, Byram BC, Dahl JJ. Short-lag spatial coherence of backscattered echoes: Imaging characteristics. IEEE Trans Ultrason Ferroelectr Freq Control 2011;58:1377–1388. [PubMed: 21768022]

Lenox MW, Wiskin J, Lewis MA, Darrouzet S, Borup D, Hsieh S. Imaging performance of quantitative transmission ultrasound. Int J Biomed Imaging 2015;2015 454028. [PubMed: 26604918]

Long W, Bottenus N, Trahey GE. Lag-one coherence as a metric for ultrasonic image quality. IEEE Trans Ultrason Ferroelectr Freq Control 2018;65:1768–1780. [PubMed: 30010556]

Long W, Bottenus N, Trahey GE. Incoherent clutter suppression using lag-one coherence. IEEE Trans Ultrason Ferroelectr Freq Control 2020;67:1544–1557. [PubMed: 32142428]

Malik BH, Klock JC. Breast cyst fluid analysis correlations with speed of sound using transmission ultrasound. Acad Radiol 2019;26:76–85. [PubMed: 29887398]

Malik B, Klock J, Wiskin J, Lenox M. Objective breast tissue image classification using quantitative transmission ultrasound tomography. Sci Rep 2016;6:1–8. [PubMed: 28442746]

Mallart R, Fink M. The Van Cittert Zernike theorem in pulse echo measurements. J Acoust Soc Am 1991;90:2718–2727.

Mandelson MT, Oestreicher N, Porter PL, White D, Finder CA, Taplin SH, White E. Breast density as a predictor of mammographic detection: Comparison of interval- and screen-detected cancers. J Natl Cancer Inst 2000;92:1081–1087. [PubMed: 10880551]

Mendelson EB, Berg WA, Merritt CR. Toward a standardized breast ultrasound lexicon, BI-RADS: Ultrasound. Semin Roentgenol 2001;36:217–225. [PubMed: 11475068]

Mesurolle B, Bining HJ, Khoury ME, Barhdadi A, Kao E. Contribution of tissue harmonic imaging and frequency compound imaging in interventional breast sonography. J Ultrasound Med 2006;25:845–855. [PubMed: 16798895]

Nahiyan A, Hasan MK. Hybrid algorithm for elastography to visualize both solid and fluid-filled lesions. Ultrasound Med Biol 2015;41: 1058–1078. [PubMed: 25701523]

Nair AA, Tran TD, Bell MAL. Robust short-lag spatial coherence imaging. IEEE Trans Ultrason Ferroelectr Freq Control 2018;65: 366–377. [PubMed: 29505405]

Nair AA, Washington KN, Tran TD, Reiter A, Bell MAL. Deep learning to obtain simultaneous image and segmentation outputs from a single input of raw ultrasound channel data. IEEE Trans Ultrason Ferroelectr Freq Control 2020;67:2493–2509. [PubMed: 32396084]

Nam K, Zagzebski JA, Hall TJ. Quantitative assessment of in vivo breast masses using ultrasound attenuation and backscatter. Ultrason Imaging 2013;35:146–161. [PubMed: 23493613]

Nightingale KR, Kornguth PJ, Trahey GE. The use of acoustic streaming in breast lesion diagnosis: A clinical study. Ultrasound Med Biol 1999;25:75–87. [PubMed: 10048804]

Oelze ML, Jr O'Brien WD, Zachary JF. 11B-4 quantitative ultrasound assessment of breast cancer using a multiparameter approach. Proc IEEE Ultrason Symp 2007;981–984.

Phillips AV, Torres G, Steed D, Caughey MC, Merhout J, Kirk SR, Hartman TS, Kuzmiak CM, Ray EM, Gallippi CM. ARFI variance of acceleration for diagnostic breast cancer imaging in women, in vivo. Proc IEEE Int Ultrason Symp 2021;1–3.

Rabbi MSE, Hasan MK. Speckle tracking and speckle content based composite strain imaging for solid and fluid filled lesions. Ultrasonics 2017;74:124–139. [PubMed: 27771558]

Rosen EL, Soo MS. Tissue harmonic imaging sonography of breast lesions: Improved margin analysis, conspicuity, and image quality compared to conventional ultrasound. Clin Imaging 2001;25:379–384. [PubMed: 11733148]

Sadeghi-Naini A, Papanicolau N, Falou O, Zubovits J, Dent R, Verma S, Trudeau M, Boileau JF, Spayne J, Iradji S, Sofroni E, Lee J, Lemon-Wong S, Yaffe M, Kolios MC, Czarnota GJ. Quantitative ultrasound evaluation of tumor cell death response in locally advanced breast cancer patients receiving chemotherapy. Clin Cancer Res 2013;19:2163–2174. [PubMed: 23426278]

Sannachi L, Tadayyon H, Sadeghi-Naini A, Tran W, Gandhi S, Wright F, Oelze M, Czarnota G. Non-invasive evaluation of breast cancer response to chemotherapy using quantitative ultrasonic backscatter parameters. Med Image Anal 2015;20:224–236. [PubMed: 25534283]

Shankar PM, Dumane V, Reid JM, Genis V, Forsberg F, Piccoli CW, Goldberg BB. Classification of ultrasonic B-mode images of breast masses using Nakagami distribution. IEEE Trans Ultrason Ferroelectr Freq Control 2001;48:569–580. [PubMed: 11370371]

Shin B, Jeon S, Ryu J, Kwon HJ. Elastography for portable ultrasound. Biomed Eng Lett 2018;8:101–116. [PubMed: 30603195]

Siegel RL, Miller KD, Fuchs HE, Jemal A. Cancer statistics, 2022. CA Cancer J Clin 2022;72:7–33. [PubMed: 35020204]

Soo MS, Ghate SV, Baker JA, Rosen EL, Walsh R, Warwick BN, Ramachandran A, Nightingale KR. Streaming detection for evaluation of indeterminate sonographic breast masses: A pilot study. Am J Roentgenol 2006;186:1335–1341. [PubMed: 16632728]

Spak DA, Plaxco J, Santiago L, Dryden M, Dogan B. BI-RADS® fifth edition: A summary of changes. Diagn Interv Imaging 2017;98: 179–190. [PubMed: 28131457]

Szopinski KT, Pajk AM, Wysocki M, Amy D, Szopinska M, Jakubowski W. Tissue harmonic imaging: Utility in breast sonography. J Ultrasound Med 2003;22:479–487. [PubMed: 12751859]

Trop I, Destrempes F, El Khoury M, Robidoux A, Gaboury L, Allard L, Chayer B, Cloutier G. The added value of statistical modeling of backscatter properties in the management of breast lesions at us. Radiology 2014;275:666–674. [PubMed: 25496215]

U.S. Cancer Statistics Working Group. U.S. Cancer Statistics Data Visualizations Tool, based on 2020 submission data (1999 2018): U.S. Department of Health and Human Services. : Centers for Disease Control and Prevention and National Cancer Institute; 2021.

Wiacek A, Falomo E, Myers K, Rindal OMH, Fabrega-Foster K, Harvey S, Bell MAL. Clinical feasibility of coherence-based beamforming to distinguish solid from fluid hypoechoic breast masses. Proc IEEE Int Ultrason Symp 2018;1–4.

Wiacek A, Rindal OMH, Falomo E, Myers K, Fabrega-Foster K, Harvey S, Bell MAL. Robust short-lag spatial coherence imaging of breast ultrasound data: Initial clinical results. IEEE Trans Ultrason Ferroelectr Freq Control 2018;66:527–540. [PubMed: 30507500]

Wiacek A, Gonzalez E, Dehak N, Bell MAL. CohereNet: A deep learning approach to coherence-based beamforming. Proc IEEE Int Ultrason Symp 2019;287–290.

Wiacek A, Gonzalez E, Bell MAL. CohereNet: A deep learning architecture for ultrasound spatial correlation estimation and coherence-based beam-forming. IEEE Trans Ultrason Ferroelectr Freq Control 2020;67:2574–2583. [PubMed: 32203018]

Wiacek A, Oluyemi E, Myers K, Mullen L, Bell MAL. Coherence-based beam-forming improves the diagnostic certainty of breast ultrasound exams. Proc IEEE Int Ultrason Symp 2020;1–4.

Wiacek A, Oluyemi E, Myers K, Mullen L, Bell MAL. Coherence-based beam-forming increases the diagnostic certainty of distinguishing fluid from solid masses in breast ultrasound exams. Ultrasound Med Biol 2020;46:1380–1394. [PubMed: 32122720]

Wiacek A, Dehak N, Bell MAL. Extending CohereNet to retain physical features when classifying benign or malignant breast masses. Proc IEEE Int Ultrason Symp 2021;1–3.

Wiacek A, Oluyemi E, Myers K, Ambinder E, Bell MAL. Quantifying the impact of breast density on the lag-one coherence of hypoechoic masses. Proc IEEE Int Ultrason Symp 2021;1–4.

Wildeboer R, van Sloun R, Mannaerts CK, Salomon G, Wijkstra H, Mischi M. Synthetic elastography from B-mode ultrasound through deep learning. Proc IEEE Int Ultrason Symp 2019;108–110.

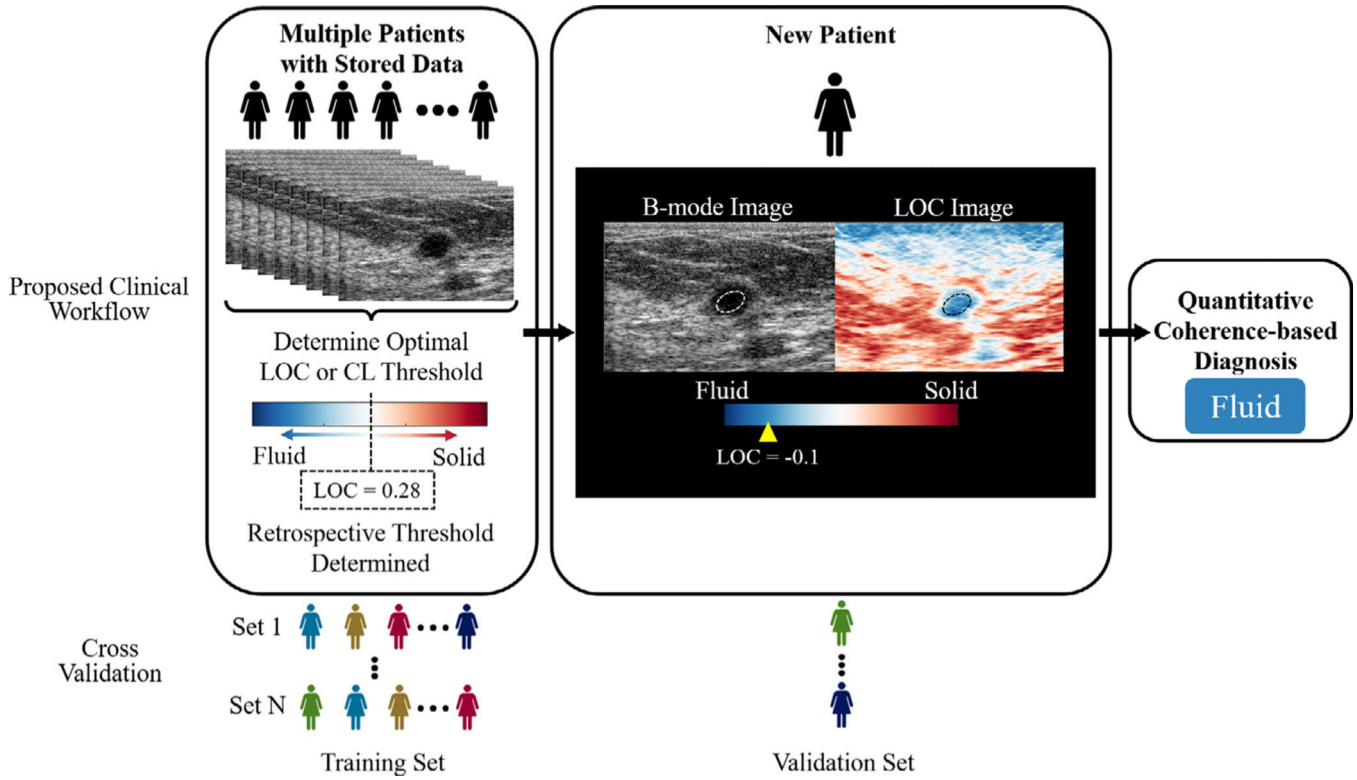

Fig. 1.

Diagram summarizing (top) the proposed clinical workflow for implementing quantitative coherence-based metrics and (bottom) the leave-one-out cross-validation to assess the feasibility of the proposed approach. CL = coherence length; LOC = lag-one coherence.

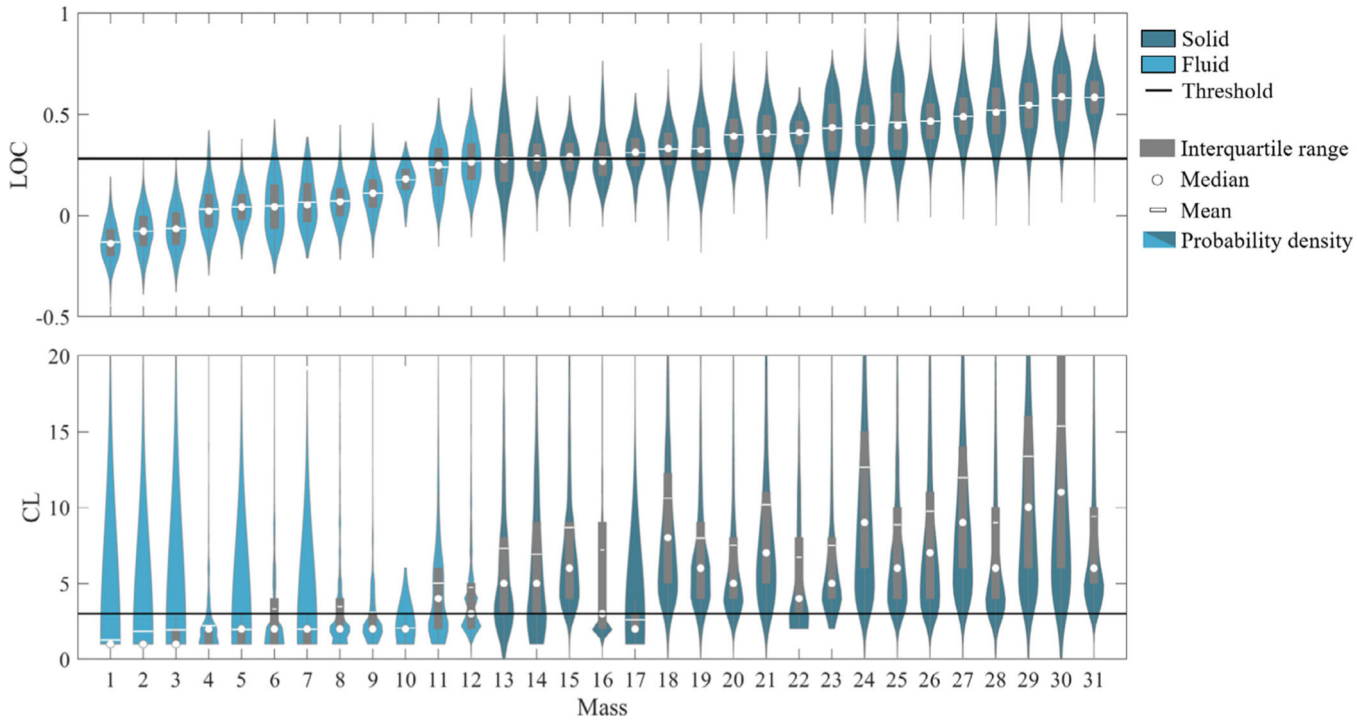

Fig. 2.

Violin plots showing (top) LOC and (bottom) CL values for each mass in this study. The shape of the shaded colors represents the probability density of the characterized data, each *solid gray box* indicates the interquartile range, each *open circle* denotes the median, each *horizontal white line* denotes the mean, and the *horizontal black line* denotes the ideal LOC or CL threshold determined from all patients. The mass type for each mass number is listed in Table 2. CL = coherence length; LOC = lag-one coherence.

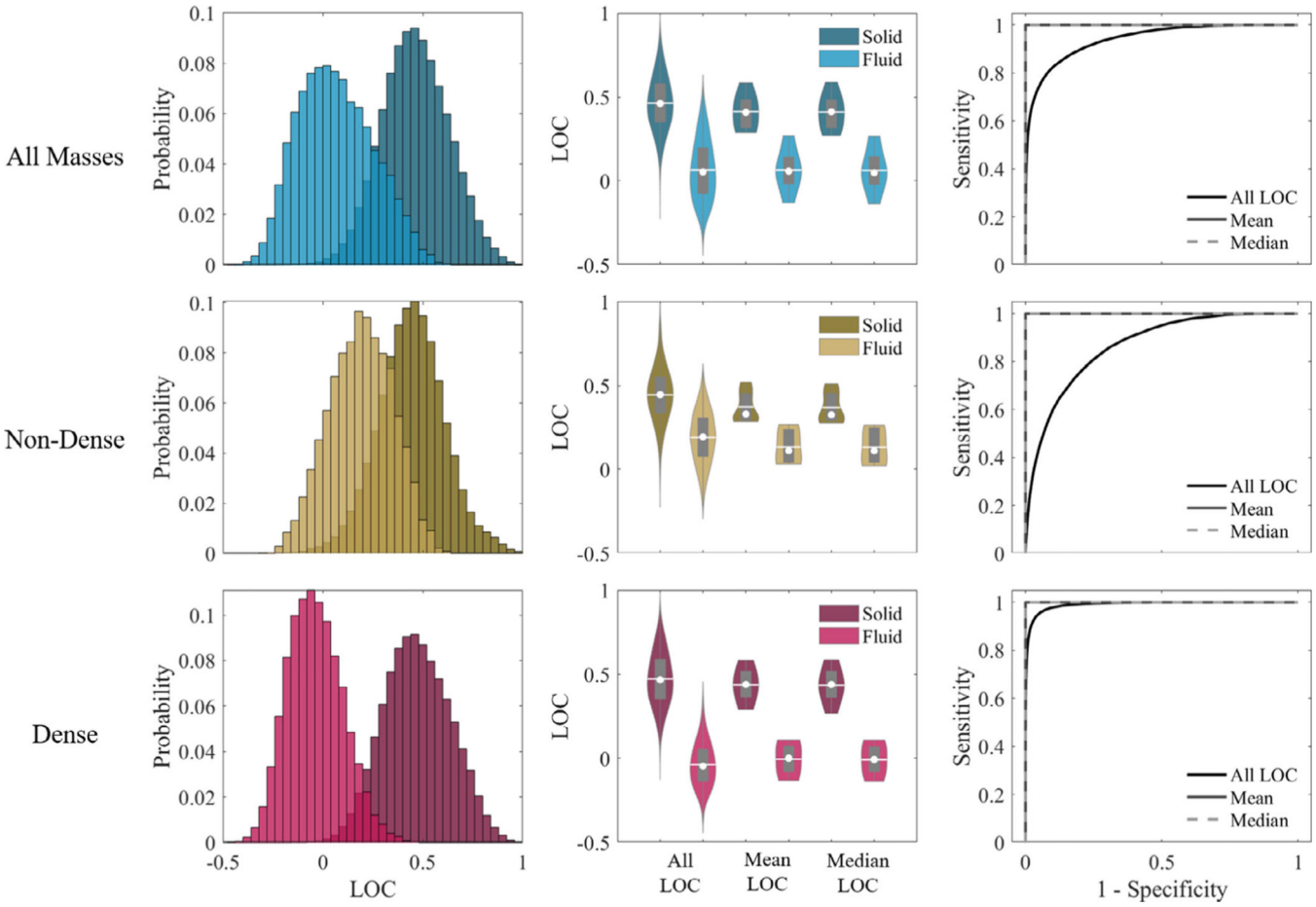

Fig. 3.

(Left) Histograms of the distribution of LOC values separated by solid and fluid masses. (Center) Violin plots of the distribution of all, mean and median LOC values. (Right) Corresponding ROC curves indicating classification performance for (top) all masses in the study, (middle) masses surrounded by non-dense breast tissue, and (bottom) masses surrounded by dense breast tissue. Note the overlap between ROC curves describing the mean and median LOC classification performance. CL = coherence length; LOC = lag-one coherence; ROC = receiver operating characteristic.

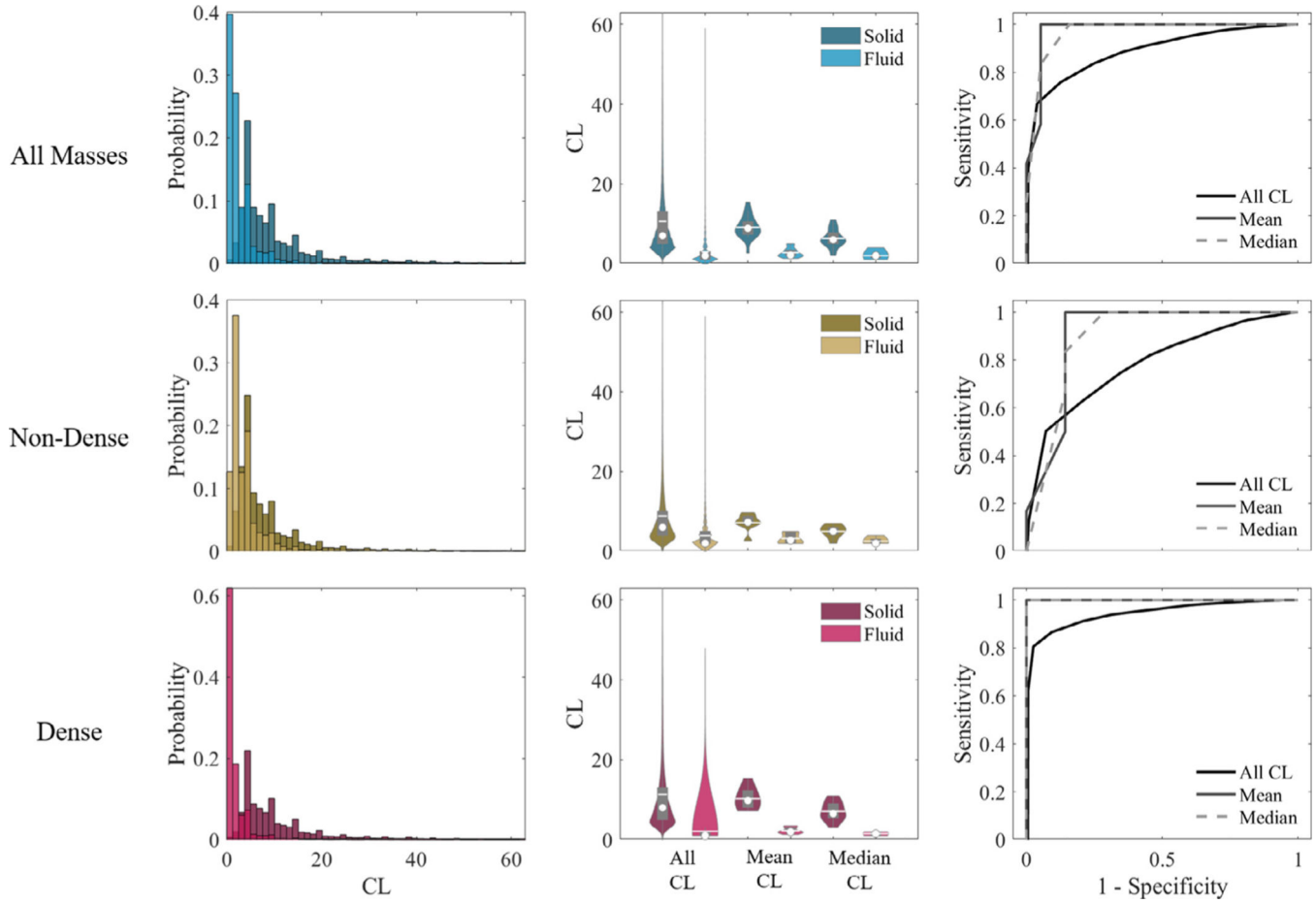

Fig. 4.

(Left) Histograms of the distribution of CL values separated by solid and fluid masses. (Center) Violin plots of the distribution of all, mean and median CL values. (Right) Corresponding ROC curves indicating classification performance for (top) all masses in the study, (middle) masses surrounded by non-dense breast tissue, and (bottom) masses surrounded by dense breast tissue. Note the overlap between ROC curves describing the mean and median CL classification performance in the bottom right plot. CL = coherence length; LOC = lag-one coherence; ROC = receiver operating characteristic.

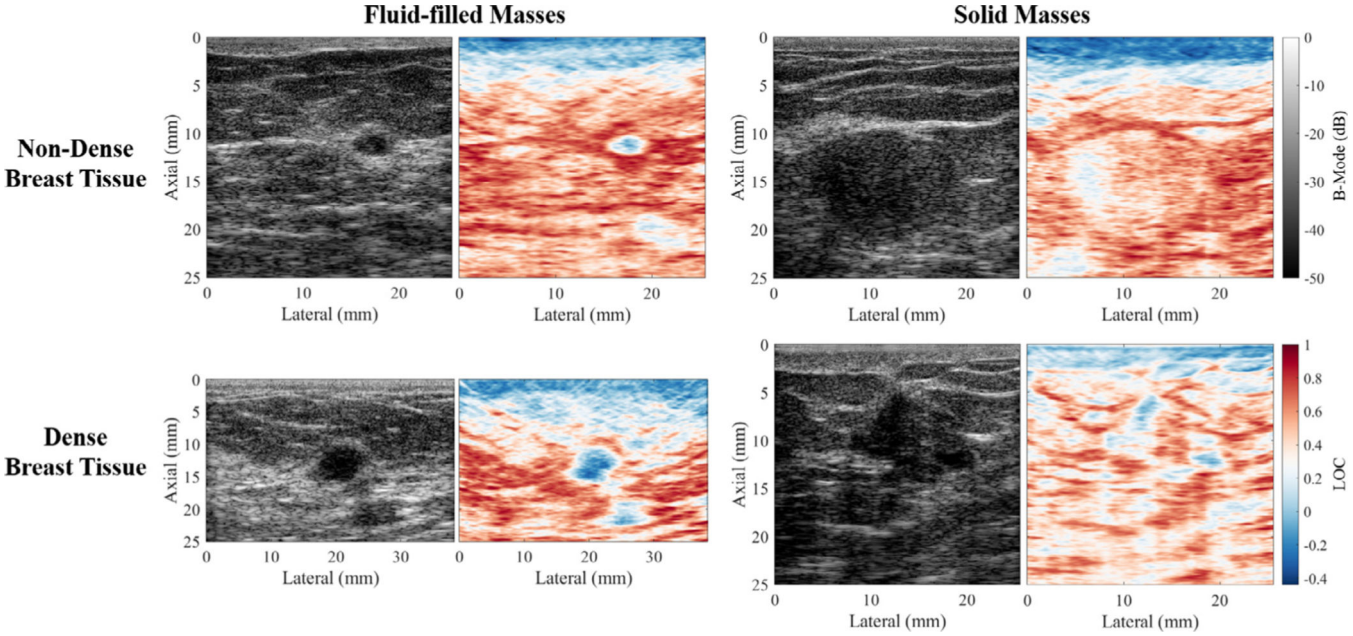

Fig. 5.

B-Mode and LOC images of (left) two fluid-filled and (right) two solid masses surrounded by (top) non-dense and (bottom) dense breast tissue. LOC = lag-one coherence.

Table 1.

Number of masses in each tissue density category.

Mass Content	Breast Tissue Density		
	Non-Dense	Dense	Total
Fluid	6	6	12
Solid	7	12	19

Table 2.

Mean and median LOC and CL values for all masses included in this study.

Mass number*	Mass type	Mean LOC	Median LOC	Mean CL	Median CL
1	Simple cyst	−0.131	−0.137	1.274	1
2	Complicated cyst	−0.077	−0.077	1.851	1
3	Complicated cyst	−0.064	−0.065	1.933	1
4	Simple cyst	0.031	0.022	2.214	2
5	Simple cyst	0.043	0.042	1.953	2
6	Simple cyst	0.048	0.043	3.318	2
7	Simple cyst	0.066	0.052	1.975	2
8	Complicated cyst	0.072	0.068	3.459	2
9	Complicated cyst	0.110	0.110	3.085	2
10	Simple cyst	0.176	0.180	2.057	2
11	Complicated cyst	0.239	0.247	5.001	4
12	Complicated cyst	0.267	0.265	4.732	3
13	Ductal carcinoma *in situ*	0.287	0.276	7.296	5
14	Apocrine metaplasia	0.287	0.284	6.916	5
15	Fibroadenoma	0.290	0.291	8.660	6
16	Invasive ductal carcinoma	0.290	0.268	7.194	3
17	Apocrine metaplasia	0.311	0.313	2.600	2
18	Fibroepithelial lesion	0.328	0.333	10.596	8
19	Ductal carcinoma *in situ*	0.330	0.325	7.976	6
20	Fibroadenolipoma	0.399	0.392	7.505	5
21	Invasive ductal carcinoma	0.401	0.407	10.165	7
22	Invasive lobular carcinoma	0.408	0.412	6.724	4
23	Invasive ductal carcinoma	0.433	0.436	7.490	5
24	Fibroadenoma	0.447	0.443	12.648	9
25	Myxoid fibroadenoma	0.461	0.445	8.858	6
26	Fibroadenoma	0.466	0.467	9.748	7
27	Fibroadenoma	0.491	0.489	11.961	9
28	Invasive ductal carcinoma	0.521	0.510	8.980	6

Mass number*	Mass type	Mean LOC	Median LOC	Mean CL	Median CL
29	Fibroadenoma	0.544	0.546	13.376	10
30	Fibroadenoma	0.581	0.587	15.349	11
31	Ductal carcinoma *in situ*	0.584	0.585	9.392	6

CL = coherence length; LOC = lag-one coherence.

*The mass number corresponds to the mass number in Figure 2.

Table 3.

Sensitivity, specificity, AUC, and optimal threshold for fluid-filled mass detection using LOC or CL.*

Breast tissue type	Method	Distribution statistic	Sensitivity	Specificity	AUC	Optimal threshold
Dense and non-dense (*i.e.*, all)	LOC	All values	0.85	0.87	0.94	0.28
		Mean values	1.00	1.00	1.00	0.28
		Median values	1.00	1.00	1.00	0.27
	CL	All values	0.76	0.87	0.89	3
		Mean values	1.00	0.95	0.97	6
		Median values	0.92	0.89	0.97	3
Non-dense	LOC	All values	0.79	0.77	0.87	0.33
		Mean values	1.00	1.00	1.00	0.28
		Median values	1.00	1.00	1.00	0.27
	CL	All values	0.63	0.79	0.78	3
		Mean values	1.00	0.86	0.90	6
		Median values	0.83	0.86	0.89	3
Dense	LOC	All values	0.95	0.95	0.99	0.21
		Mean values	1.00	1.00	1.00	0.12
		Median values	1.00	1.00	1.00	0.12
	CL	All values	0.87	0.91	0.94	3
		Mean values	1.00	1.00	1.00	4
		Median values	1.00	1.00	1.00	2
R-SLSC (Wiacek et al. 2020c)			0.86 [0.71–1.00]	0.95 [0.88–1.00]	—	—
QT ultrasound (Iuanow et al. 2017)			0.93 [0.83–1.0]	0.86 [0.79–0.95]	—	—

AUC = area under the receiver operating characteristic curve; CL = coherence length; LOC = lag-one coherence; QT = quantitative transmission; R-SLSC = robust short-lag spatial coherence.

*These objective results are compared with the mean [range] sensitivity and specificity of R-SLSC and QT ultrasound (*i.e.,* two recently investigated, reader-dependent methods).

Table 4.

Accuracy of the leave-one-out cross-validation analysis and mean ± one standard deviation of the thresholds determined from 31 training sets each containing 30 masses.

	Accuracy	Threshold
Mean LOC	96.8%	0.2754 ± 0.0054
Median LOC	96.8%	0.2660 ± 0.0018
Mean CL	93.6%	5.9677 ± 0.1796
Median CL	83.9%	3.9677 ± 0.3145

CL = coherence length; LOC = lag-one coherence.